

## Fast particle losses due to NTMs and magnetic field ripple

**E Strumberger<sup>1</sup>, S Günter, E Schwarz, C Tichmann and the ASDEX Upgrade Team**

Max-Planck-Institut für Plasmaphysik, IPP-Euratom Association  
85748 Garching, Germany

E-mail: [Erika.Strumberger@ipp.mpg.de](mailto:Erika.Strumberger@ipp.mpg.de)

*New Journal of Physics* **10** (2008) 023017 (21pp)

Received 18 September 2007

Published 13 February 2008

Online at <http://www.njp.org/>

doi:10.1088/1367-2630/10/2/023017

**Abstract.** We present a detailed numerical study of the interaction between fast particles and large-scale magnetic perturbations and toroidal field ripple. In particular we focus our study on the losses of fast ions created by neutral beam injection (NBI) for an ASDEX Upgrade discharge with neoclassical tearing mode (NTM) activity. For these investigations, we use as input an equilibrium carefully reconstructed from experimental data. The magnetic field ripple is self-consistently included by a three-dimensional, free-boundary equilibrium computation. The magnetic islands caused by a (2,1)-NTM are introduced by a field perturbation superimposed on the equilibrium magnetic field. The experimental data are used to reproduce size and location of those islands numerically. Starting from a realistic seed distribution, the guiding centres of about 100 000 fast ions are traced up to a given time limit, or until they hit plasma-facing structures. A detailed analysis of the particle trajectories provides important information on the underlying loss mechanisms such as: (i) losses of passing particles caused by drift island formation, and (ii) losses of trapped particles due to stochastic diffusion.

<sup>1</sup> Author to whom any correspondence should be addressed.

**Contents**

<b>1. Introduction</b>	<b>2</b>
<b>2. Numerical method</b>	<b>3</b>
<b>3. Magnetic islands and toroidal field ripple</b>	<b>7</b>
<b>4. Fast particle losses</b>	<b>8</b>
4.1. Initial particle distribution . . . . .	8
4.2. Passing particle losses . . . . .	10
4.3. Trapped particle losses . . . . .	15
4.4. Total losses . . . . .	18
<b>5. Summary</b>	<b>19</b>
<b>Acknowledgments</b>	<b>20</b>
<b>References</b>	<b>20</b>

**1. Introduction**

High-energy particles play an important role for plasma heating and current drive. Therefore, good confinement of those particles is essential for a successful operation of future fusion devices, such as ITER and DEMO. In toroidal magnetic field configurations particles are either passing around the torus, or they are trapped in magnetic mirrors. Neglecting energy and pitch angle scattering processes, both types of particles are confined in axisymmetric, toroidal magnetic field configurations. In tokamak devices the limited number of toroidal field coils leads to a magnetic field ripple in the toroidal direction, so that the perfect axisymmetry is violated, and trapped particles become lost due to stochastic diffusion and/or ripple well trapping [1, 2]. Further losses may occur due to the interaction of fast particles with magnetohydrodynamic (MHD) instabilities. Similar to the static magnetic field ripple, low-frequency perturbations cause losses of trapped particles due to stochastic diffusion [3]. Furthermore, experiments [4]–[6] and theoretical considerations [7, 8] have shown that high-energy passing particles are lost because of their interactions with high-frequency perturbations, such as toroidal Alfvén eigenmodes (TAEs). However, more recent experiments [9]–[12] have revealed that almost static, low-frequency MHD modes, such as neoclassical tearing modes (NTMs), also cause losses of fast passing particles. For those losses various mechanisms are currently under discussion. For instance, the overlap of drift islands of passing particles may lead to orbit stochasticity and, hence, may cause a loss of these particles [11]–[14]. Furthermore, barely passing particles may become trapped and possibly lost in fields perturbed by MHD instabilities (e.g. NTMs) [15].

New insights into the interactions between fast particles and large-scale magnetic perturbations have been gained by measurements of the fast ion loss detector (FILD) [12, 16] installed in ASDEX Upgrade. A CCD camera and an array of photomultipliers with a bandwidth of 1 MHz allow a high time resolution which has clearly shown frequency and phase correlations between particle losses and low-frequency MHD fluctuations. These experiments have motivated the numerical studies presented in this paper.

Fast orbit losses in the presence of large-scale, static, helical perturbations have already been studied analytically and numerically in other papers [12, 17, 18]. While these studies are based on axisymmetric model equilibria with circular cross-sections and/or limited to

the plasma region, we investigate a real ASDEX Upgrade equilibrium (discharge #21089 at  $t = 4$  s) including the magnetic field ripple produced by the 16 toroidal field coils of ASDEX Upgrade. The field ripple is self-consistently included by a three-dimensional (3D), free-boundary equilibrium computation. The magnetic field perturbation caused by a (2,1)-NTM, which has been observed at this time [12], is superimposed on the equilibrium field. The field perturbation is computed from the perturbed poloidal flux, for which we use an analytical ansatz. The free parameters of this ansatz are chosen in such a way that radial location and width of the (2,1)-islands are consistent with the motional Stark effect (MSE) and electron cyclotron emission (ECE) measurements. Starting from a realistic seed distribution, the guiding centres of about 100 000 fast ions are traced up to a given time limit, or until they hit plasma-facing components (PFCs), such as limiter and divertor structures. In other words, the tracing of the guiding centres is not limited to the plasma region, but is continued beyond the separatrix. A detailed analysis of the particle trajectories will then provide important information on the underlying loss mechanisms. Although a quantitative comparison with experimental data is beyond the scope of our studies, the results qualitatively agree with the FILD measurement [12].

The paper is organized as follows. The numerical method is briefly described in section 2. In section 3, the magnetic field topology including magnetic islands and field ripple is studied for the ASDEX Upgrade discharge #21089 at  $t = 4$  s. In section 4, the initial particle distribution is described (section 4.1), and various types of fast ion guiding centre trajectories and loss mechanisms are investigated for passing (section 4.2), and trapped particles (section 4.3). The total particle losses are discussed in section 4.4. Finally, in section 5 we summarize the work.

## 2. Numerical method

The ASDEX Upgrade discharge #21089 at  $t = 4$  s (vacuum magnetic field  $B_0 = 2$  T, total plasma current  $I_p = 0.8$  MA) was unstable with respect to NTMs. Around the magnetic surface with safety factor  $q = 2$  large (2,1)-islands formed with a width of approximately 12 cm. The perturbation led to an increased loss of fast particles measured with the newly installed FILD [12, 16]. This discharge is the basis of our studies presented below. The corresponding equilibrium is carefully reconstructed from experimental data with the axisymmetric CLISTE equilibrium reconstruction code [19, 20] taking into account MSE measurements. We recalculate the unperturbed equilibrium with the 3D, free-boundary VMEC/NEMEC code [21, 22] twice. In one study, we use an axisymmetric approximation of the toroidal field, and in the other we take into account the 3D toroidal field produced by the 16 toroidal field coils of ASDEX Upgrade. The latter calculation yields the 3D equilibrium with magnetic field ripple.

Figure 1 shows a cross-section of the unperturbed, axisymmetric equilibrium. In agreement with the MSE data the  $q = 2$  surface is located at approximately 60% of the plasma radius. This figure also shows the separatrix, the poloidal position of the FILD, and an outer limiting surface. In order to avoid the numerical effort connected with the determination of the positions where the guiding centres of the fast ions hit the 3D wall structures, we approximate the PFCs by an axisymmetric, closed surface. This simplification is appropriate and sufficient for our goal to identify the various loss mechanisms.

Up to the outer limiting surface the axisymmetric and 3D, unperturbed magnetic fields are computed with the MFBE code [23, 24] in cylindrical co-ordinates on a grid. In order to simulate the magnetic islands caused by the NTM, a magnetic field perturbation,  $\mathbf{B}_{\text{pert}} = \nabla \tilde{\Psi} \times \nabla \varphi$ , is superimposed on to the equilibrium field. For the perturbed poloidal flux,  $\tilde{\Psi}$ , we make the

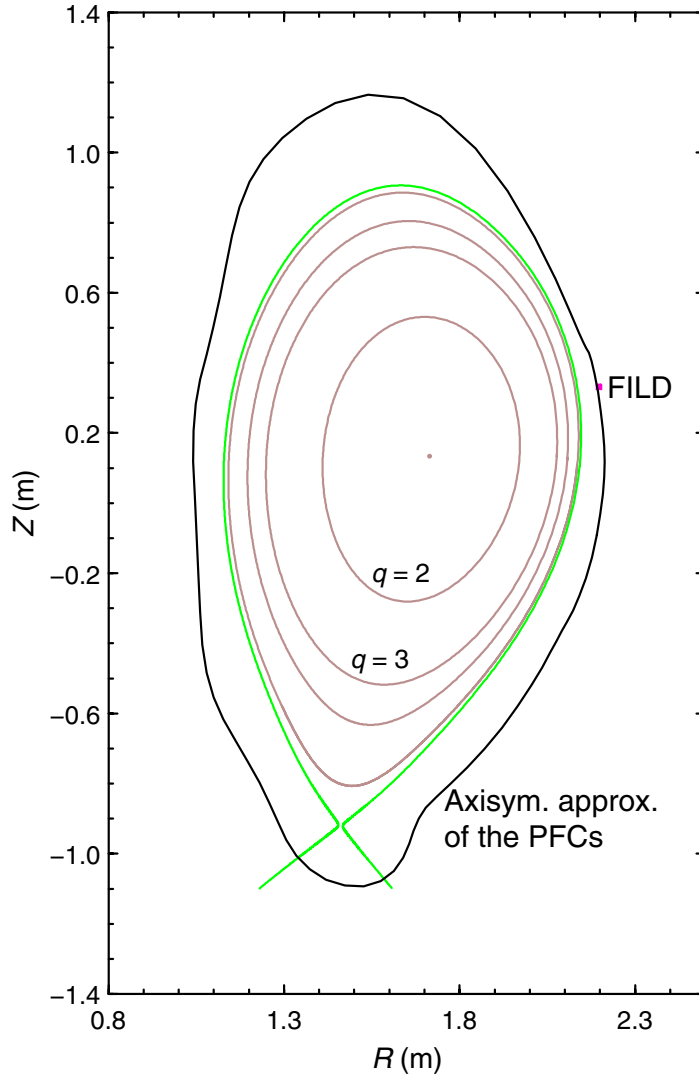


**Figure 1.** Cross-section of the equilibrium of discharge #21089 at  $t = 4$  s showing the rational surfaces with  $q = 2, 3, 4$  and  $5$  (brown lines), the separatrix (green line), the poloidal position of the FILD (magenta square), as well as the axisymmetric approximation of the PFCs (black line).

following analytical ansatz:

$$\tilde{\Psi}(s, \vartheta, \varphi) = \sum_{m,n} A_{m,n}(s) \cos(m\vartheta - n\varphi - \phi_{m,n}), \quad (1)$$

which is a function of the flux co-ordinates  $s, \vartheta, \varphi$ . These co-ordinates are the normalized toroidal flux,  $s$ , a poloidal angle co-ordinate,  $\vartheta$ , and the toroidal angle,  $\varphi$ . The latter is the toroidal angle in cylindrical co-ordinates. The variables  $m$  and  $n$  are the poloidal and toroidal harmonics of the perturbation. Here we only consider  $m = 2$  and  $n = 1$ . At this point, it should be noted that in a realistic tokamak geometry this perturbation also causes islands of higher order, such as  $(3,1)$ ,  $(4,1)$  and so on (see figure 5). The variable  $\phi_{m,n}$  determines the island phase.

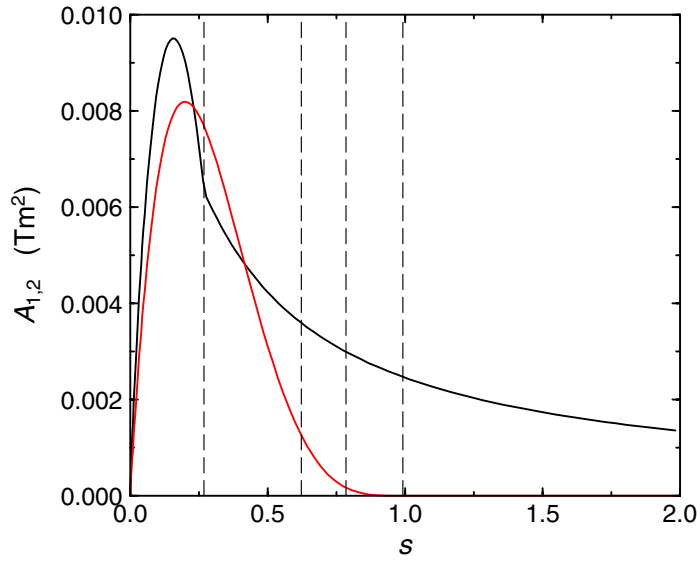


**Figure 2.** Parametrized functions,  $A_{2,1}$ , as a function of the normalized toroidal flux  $s$  for a (2,1)-mode. The black line shows the function of perturbation 1 (equations (2) and (3)), while the red line describes the radial behaviour of perturbation 2 (equation (4)). The dashed, vertical lines indicate the  $s$ -values of the rational  $q$ -values 2, 3, 4 and 5 (from left to right).

In order to study the influence of the radial profile of the magnetic perturbation on the fast particle losses, we use two different radial functions  $A_{2,1}$ . The first function [25] describes resistive modes, and does not disappear in the vacuum region. This function consists of two parts

$$A_{m,n}(s) = \rho_{m,n} \alpha \left( \frac{s}{s_{m,n}} \right)^{m/2} \left[ 1 - \beta \left( \frac{s}{s_{m,n}} \right)^{1/2} \right] \quad \text{for } s \leq s_{m,n} \quad (2)$$

and

$$A_{m,n}(s) = \rho_{m,n} \frac{\alpha(1 - \beta) - \gamma + \gamma(s/s_{m,n})^{1/2}}{(s/s_{m,n})^{(m+1)/2}} \quad \text{for } s > s_{m,n}. \quad (3)$$

The variables  $\rho_{m,n}$ ,  $\alpha$ ,  $\beta$  and  $\gamma$  are free parameters, which determine the island widths as well as the perturbation strength in the vacuum region. The variable  $s_{m,n}$  is the normalized toroidal flux of the  $q = m/n$  surface. In order to obtain the experimentally observed (2,1)-island width and position, and at least the same order of magnitude for the measured radial perturbation field strength ( $3 \times 10^{-4}$  T) in the vacuum region, we use  $\alpha = 0.04$ ,  $\beta = 0.87$ ,  $\gamma = 0.01$ ,  $\rho_{2,1} = 12 \times 10^{-4}$  and  $s_{2,1} = 0.2693$ . From now on, we will call this ansatz perturbation 1.

We also consider a second analytical expression (perturbation 2) for the radial function which disappears at the plasma boundary ( $s = 1$ ). In this ansatz [26], the radial function is defined by

$$A_{m,n}(s) = c_0 s^{k_1/2} (1 - s)^{k_2}. \quad (4)$$

Again, the free parameters  $c_0$ ,  $k_1$  and  $k_2$  are chosen in such a way that width and position of the (2,1)-islands approximate the experimental data ( $c_0 = 0.1$ ,  $k_1 = 2$ , and  $k_2 = 4$ ). Figure 2 shows the radial behaviour of both perturbations for the considered (2,1)-mode.

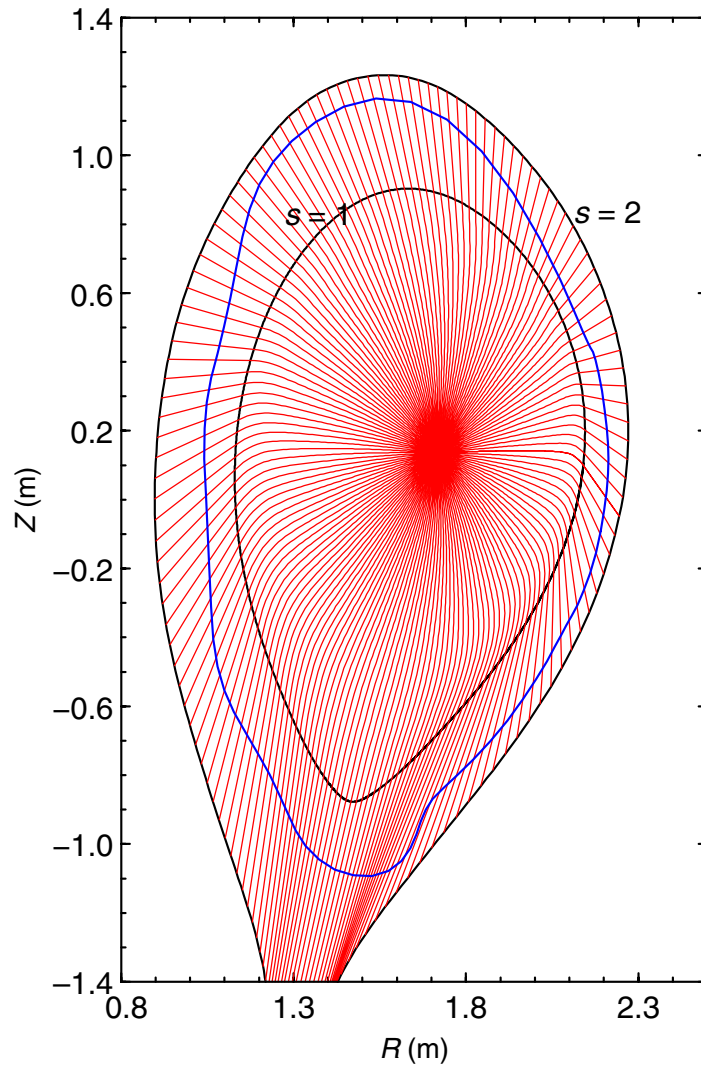


**Figure 3.** Cross-section of the extended flux co-ordinate system. The red, radial lines correspond to constant values of the poloidal co-ordinate,  $\vartheta$ , while the poloidal curves mark the plasma boundary (inner black line), the outer boundary (outer black line) obtained by extrapolation, and the outer limiting surface (blue line), which approximates the plasma-facing structures.

Since flux co-ordinates are only defined inside the plasma, it is necessary to extend this co-ordinate system into the vacuum region. Therefore, we define an outer co-ordinate surface. This surface is obtained by a radial extrapolation of the Fourier coefficients describing the shape of the plasma boundary. As shown in figure 3, this surface, which corresponds to  $s = 2$ , does not only enclose the outer limiting surface, but also allows a smooth extension of the poloidal co-ordinate lines. The MFBE code used to compute the equilibrium magnetic field is extended in order to compute also the magnetic field perturbation on the same 3D grid as the equilibrium field.

Together with an initial distribution of fast ions, and some information about plasma and wall geometries, the equilibrium and perturbation fields serve as input to the GOURDON



code [27]. We use an extended and parallelized version of this code, which is able to trace thousands of magnetic field lines or guiding centres, and which determines the positions where the guiding centres hit the outer limiting surface (for more details see [28, 29]). The initial distribution of the fast ions is computed with the FAFNER code [30], and the geometrical input is produced with the GEOM code [29]. However, up to now no particle collisions are included in the GOURDON code. For the considered particle (see section 4.1) and plasma properties (particle density:  $n \approx 6 \times 10^{19} \text{ m}^{-3}$ , ion temperature:  $T_i \approx 4.3 \text{ keV}$ , electron temperature:  $T_e \approx 2.9 \text{ keV}$  (all quantities given in the plasma centre)) the rate of change of the beam energy  $d\varepsilon/dt$  and the total deflection frequency  $\nu_d$  of the pitch angle scattering are  $d\varepsilon/dt \approx 10^6\text{--}10^7 \text{ eV s}^{-1}$  and  $\nu_d \approx 1\text{--}10 \text{ s}^{-1}$ , with the rates increasing from the plasma centre to the plasma boundary. As we will show in section 4.4, the neglect of the particle collisions is justified for the presented studies. Furthermore, we do not consider the rotation of the islands, because the transit frequencies of fast particles are much higher than the mode frequency of the (2,1)-NTM [12].

### 3. Magnetic islands and toroidal field ripple

As a first step, we compute the pure axisymmetric magnetic field, the field with toroidal field ripple, the perturbed axisymmetric fields using perturbations 1 and 2 and the fields with ripple and perturbations 1 and 2, respectively.

The toroidal magnetic field ripple and its influence on the magnetic field topology is illustrated in figures 4(a) and (b). Figure 4(a) shows the ripple strength  $\delta$ , defined by

$$\delta = \frac{B_{\max} - B_{\min}}{B_{\max} + B_{\min}}, \quad (5)$$

with  $B_{\min}$  and  $B_{\max}$  being the minimum and maximum magnetic field strength in the toroidal direction. The ripple is highest at the low-field side. At the outer midplane the ripple amounts to 0.33% at 70% of the plasma radius, and to 0.66% at the plasma boundary. The displacement of the field lines due to the field ripple is illustrated in figure 4(b). The red and black lines indicate the poloidal projection of the field lines with and without ripple. Due to the ripple the red lines show an inward/outward radial displacement. Close to the plasma boundary (green line) the radial displacement of these field lines relative to the field lines traced in the corresponding axisymmetric field varies between  $\pm 1 \text{ mm}$ . The radial displacement increases with decreasing distance to the toroidal field coils. At the position of the outer limiting surface (blue line) the radial displacement amounts to  $\pm 2 \text{ mm}$ .

Figures 5(a)–(d) show Poincaré plots of field lines traced in the magnetic fields including field ripple and perturbation fields. For both kinds of perturbations the widths of the (2,1)-islands are  $\Delta_{2,1} = 0.12 \text{ m}$ . The O-points of the islands are shifted approximately by 0.02–0.03 m inside the unperturbed  $q = 2$  surface, while the X-points are shifted outward. This behaviour has also been observed in the MSE and CEC measurements. Using perturbation 2, which disappears at the plasma boundary, the boundary region is not ergodized, and islands with  $m > 2$  are much smaller than those obtained with perturbation 1. For the latter perturbation the (3,1)- and (4,1)-island widths are  $\Delta_{3,1} = 0.024 \text{ m}$  and  $\Delta_{4,1} = 0.016 \text{ m}$ . Figures 5(a)–(d) show the cross-sections for  $\varphi = 180^\circ$ . Note that at this cross-section all O-points are aligned in the outer midplane.

These magnetic fields, as well as their axisymmetric approximations with and without perturbation, and the unperturbed field with ripple are used for the following computations of fast ion guiding centre orbits and losses. Furthermore, the perturbed fields are computed

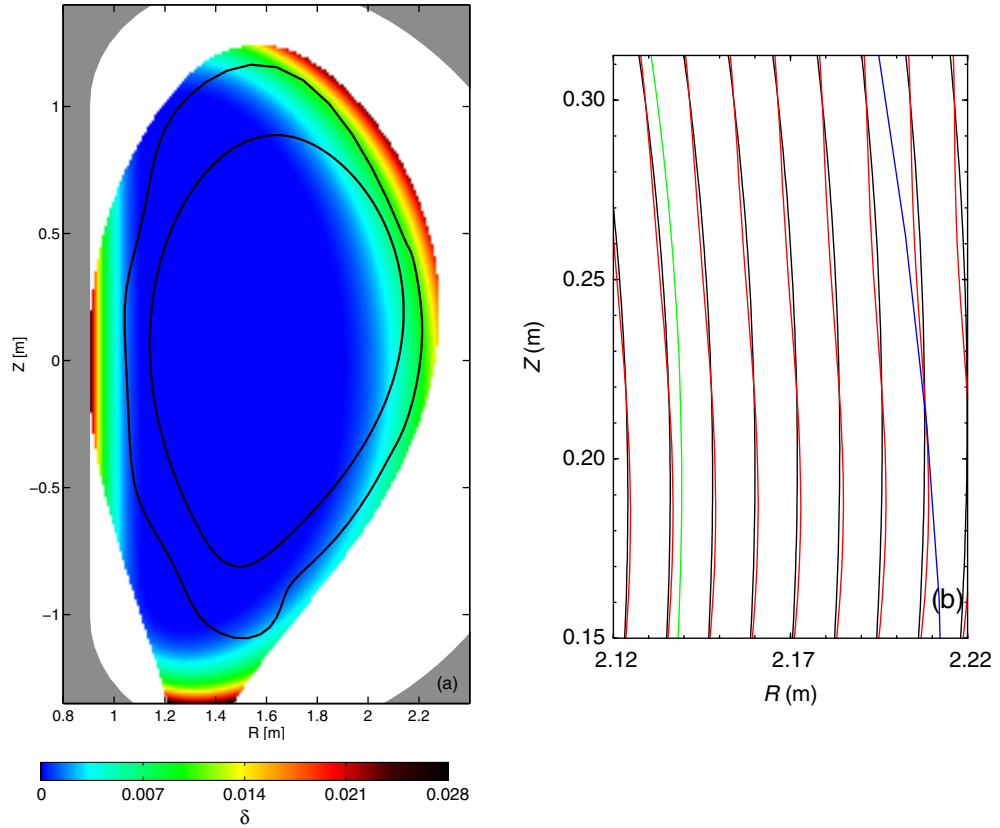


**Figure 4.** (a) Ripple strength,  $\delta$ , as function of  $R$ - and  $Z$ -coordinates. The black solid lines indicate the positions of the plasma boundary and the outer limiting surface, and the grey areas represent parts of the toroidal field coils. (b) Poloidal projection of field lines traced in magnetic fields without (black) and with ripple (red). The green and blue lines indicate the positions of the plasma boundary and the outer limiting surface, respectively. (b) shows an enlargement of the low-field region.

for various phases of the perturbations, namely  $\phi_{2,1} = 0^\circ, 45^\circ, 90^\circ, 135^\circ, 180^\circ, 225^\circ, 270^\circ$  and  $315^\circ$ .

## 4. Fast particle losses

### 4.1. Initial particle distribution

ASDEX Upgrade has a 20 MW neutral beam injection (NBI) system composed of two injectors, which are located at the low-field side. Each injector has four neutral beam sources. During discharge #21089 only three sources (#3, #5 and #7) were active. While #5 and #7 injected deuterons with  $E = 93, 46.5$  and  $31$  keV, the particle energies of #3 were  $E = 60, 30$  and  $20$  keV. The resulting initial distribution of fast ions is determined with the FAFNER code [30]. For the following studies an initial distribution of almost 100 000 particles is used, with approximately  $1/3$  of the particles produced by each source. Figure 6 presents spatial and pitch



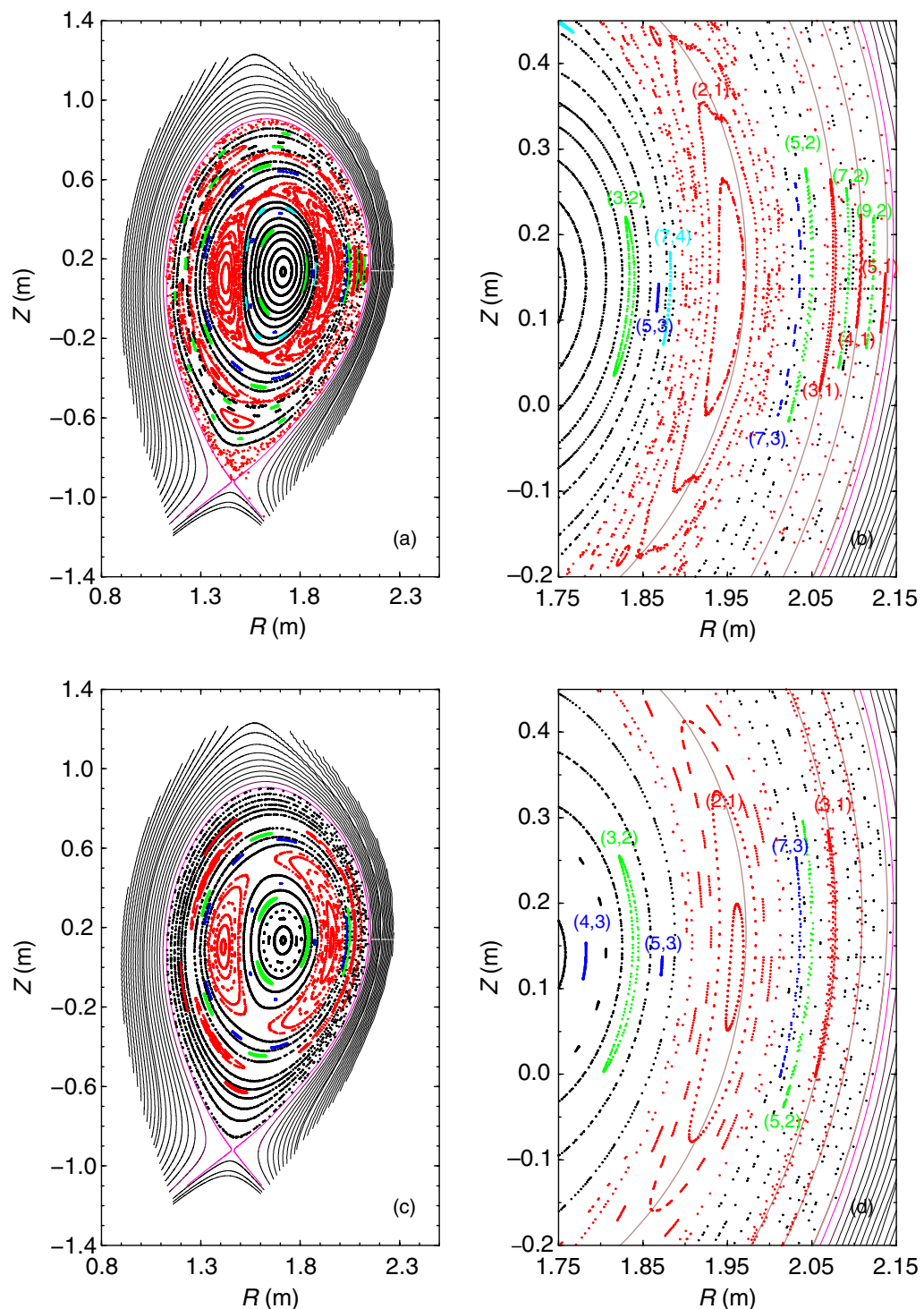


**Figure 5.** Poincaré plots of the magnetic field with ripple, and perturbations 1 (a) and (b) and 2 (c) and (d), respectively. (b), (d) Enlargements of the low field side region around the magnetic axis. There, the brown lines indicate the positions of the rational surfaces in the case of the unperturbed equilibrium, while the numbers indicate the island type.

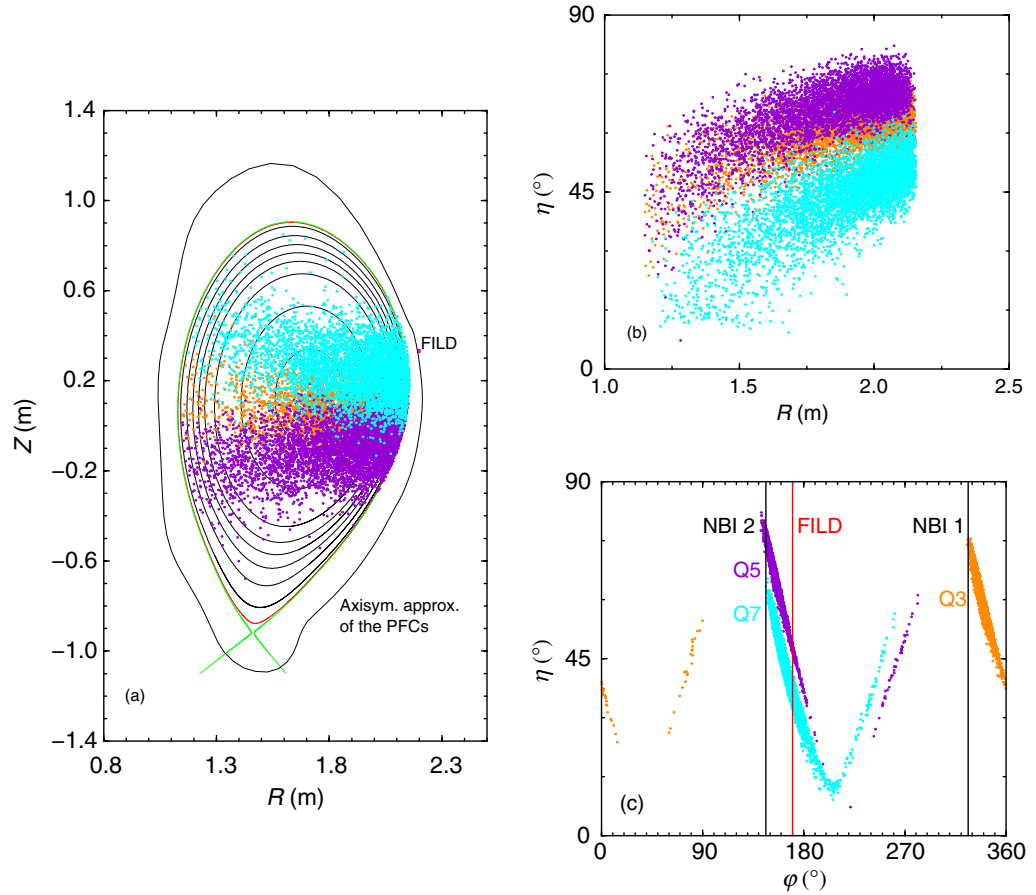


**Figure 6.** Spatial and pitch angle distributions of the injected particles of #3 (orange), #5 (violet) and #7 (cyan). Only 5000 particles of each source are plotted. (a) Poloidal projection of the particles with rational flux surfaces (inner black lines), separatrix (green), outer limiting surface (outer black line), and poloidal position of the FILD. (b), (c) Pitch angle distributions as functions of (b) the radial and (c) the toroidal co-ordinates. The vertical black and red lines mark the toroidal positions of the two neutral beam injectors and the FILD.

angle distributions of these ions. Here the pitch angle,  $\eta$ , is defined by  $\eta = \arccos(v_{\parallel}/v)$ , with  $v_{\parallel}$  and  $v$  being the parallel and total particle velocities. As shown in figure 6(a), the injected neutral particles are predominantly ionized at the low-field side, whereas a small part penetrates to the high-field side. About 54 (#3), 58 (#5) and 10% (#7) of the injected particles are trapped in magnetic mirrors. This is because particles of #7 are injected with a larger parallel velocity component than particles of #3 and #5. In figure 6, the particles injected by the sources #3, #5 and #7 are represented by the colours orange, violet and cyan. In the following, we will keep this colour code.

#### 4.2. Passing particle losses

The drift orbits of passing particles are shifted with respect to magnetic flux surfaces. In figures 7(a) and (b) the drift orbits of test particles ( $E = 93$  keV and  $\eta = 8^\circ$ ) are shown. These

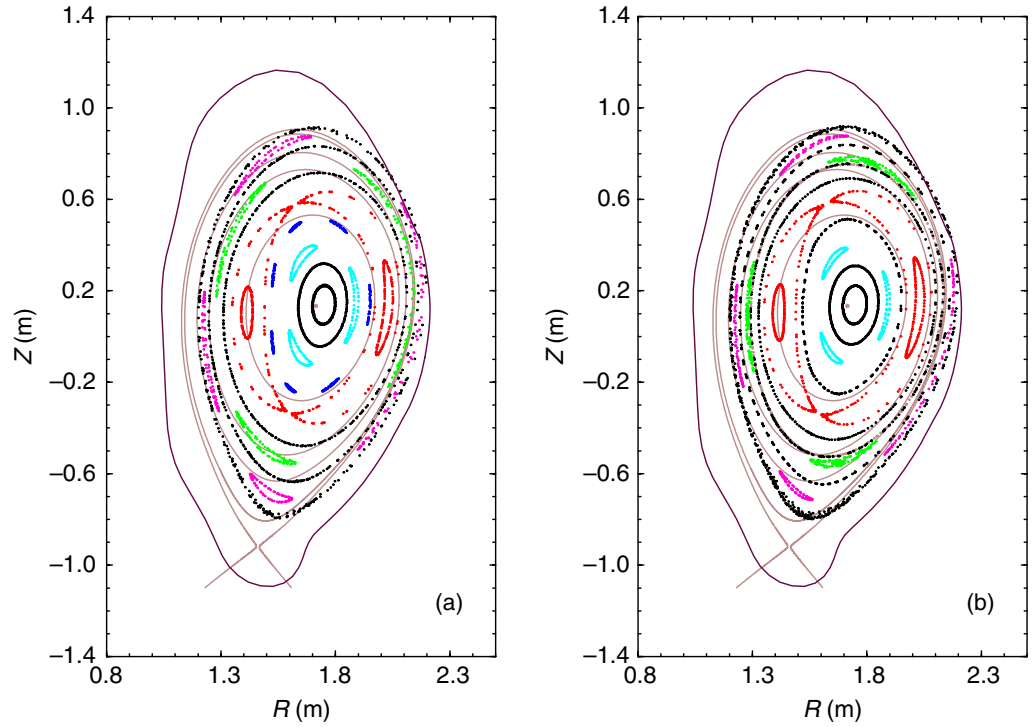


**Figure 7.** Poincaré plots of characteristic guiding centre orbits of passing particles in perturbed fields using (a) perturbation 1 and (b) perturbation 2. The brown lines show unperturbed rational flux surfaces and the separatrix. The maroon line marks the outer limiting surface.

particles are traced in magnetic fields without ripple but superimposed perturbation fields 1 and 2, respectively. Similar to the magnetic islands, the guiding centre orbits describe so-called drift islands. Here the widths of these islands are of the same size as the magnetic islands, but their positions are shifted in the outward direction (because of the directions of the magnetic field and the particle velocities). The island phases sensitively depend on the perturbation (see figures 7(a) and (b)). Regarding perturbation 1, we find a cross-section  $\varphi = 180^\circ$ , where we have a similar situation for the O-points of the drift islands as for the magnetic islands (see section 3). The O-points of all drift islands (i.e. (3,2), (2,1), etc) are located around the midplane at the low-field side. However, the (3,1)-drift islands (green dots in figures 7(a) and (b)) have a different phase for perturbation 2. There, an X-point lies on the low-field side. Note, for this specific discharge and for both perturbations we observe no significant stochasticization of the drift orbits.

There are several mechanisms responsible for passing particle losses. First, we study so-called prompt losses of passing particles in the unperturbed, axisymmetric field. These particles are lost because their drift orbits hit PFCs. In figure 8(a), we show typical guiding centre orbits of such particles. Only a small portion of the passing particles (#3: 0.3%, #5: 1.3%, #7: 0.2%) is lost into the lower divertor region. Their loss times,  $t_{\text{loss}}$ , are mostly shorter than  $15 \mu\text{s}$ , but a few of them need more time ( $t_{\text{loss}} \leq 30 \mu\text{s}$ ) to reach the divertor plates. As shown in figure 8(a), these latter particles come close to the X-point, where their motion is primarily directed in the toroidal direction. All of these lost particles have their origins close to the plasma boundary

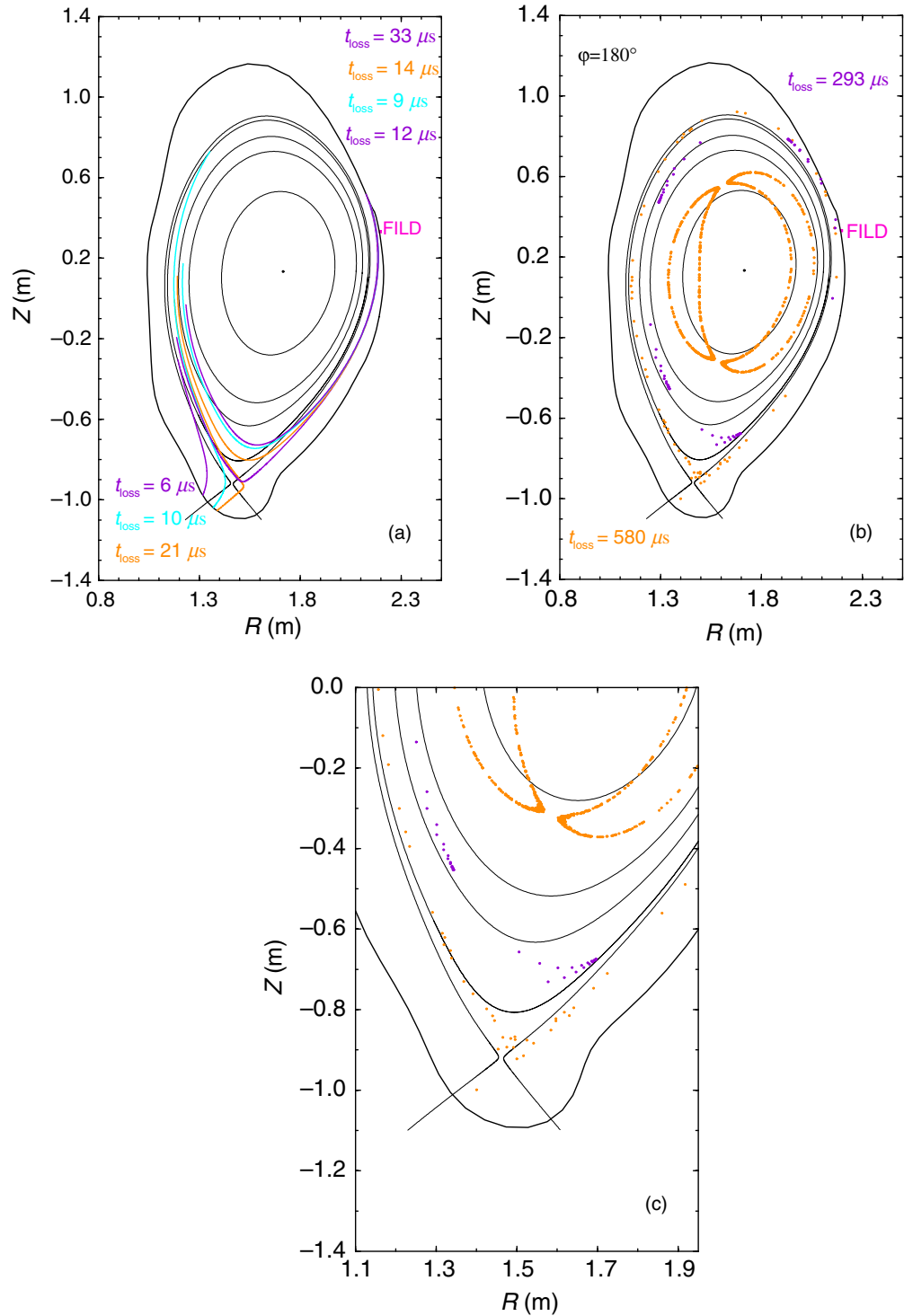


**Figure 8.** Poloidal projection (a) and Poincaré plots (b) and (c) of characteristic guiding centre orbits of passing particles (coloured lines and points) in the (a) axisymmetric field, (b) and (c) perturbed field (perturbation 1). (c) Enlargement of the lower middle section of (b). The black lines show unperturbed rational flux surfaces, the separatrix and the outer limiting surface.

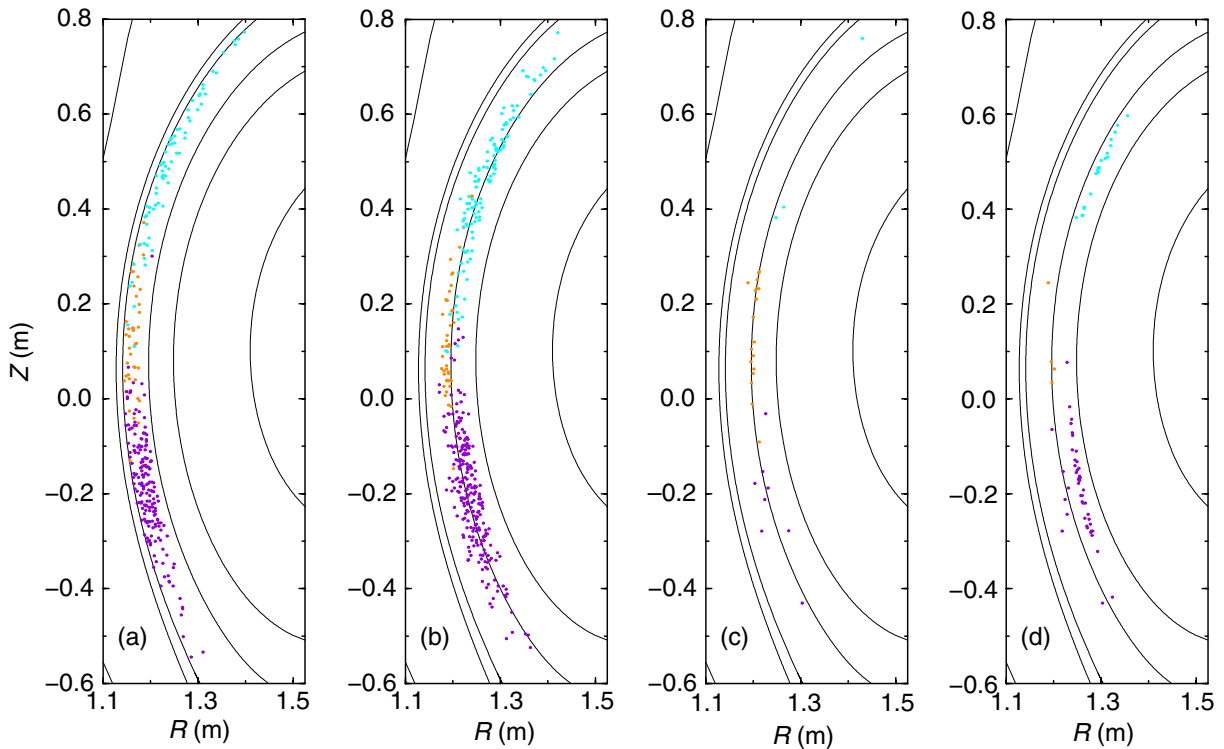


**Figure 9.** Poloidal projection of the initial distributions of the lost passing particles: (a) unperturbed axisymmetric field, particles lost in the lower divertor region, (b) unperturbed axisymmetric field, particles lost at the low-field side, (c) unperturbed field with ripple, additionally lost particles at the low-field side, (d) perturbed field (perturbation 1) without ripple, additionally lost particles at the low-field side. The black lines show unperturbed rational flux surfaces, the separatrix and the outer limiting surface.

at the high-field side (see figure 9(a)). Furthermore, the lost particles hit the outer limiting surface all over the toroidal circumference (see figure 10(a)). The number of lost particles and the deposition patterns of these particles remain almost unchanged even when field ripple and magnetic perturbation are taken into account.

In case of the axisymmetric field without perturbation, the passing particles which are lost at the low-field side need at least  $10 \mu\text{s}$ , but less than  $35 \mu\text{s}$ , to reach the outer limiting surface. Examples of typical drift orbits can be seen in figure 8(a). Again only a small portion (#3: 0.3%, #5: 1.8%, #7: 0.4%) of the passing particles is lost. However, it should be mentioned that approximately 40% more passing particles hit the outer limiting surface at the low-field side than in the lower divertor region.

Apart from prompt losses no passing particles are lost in the axisymmetric field, if particle collisions are neglected. However, due to numerical inaccuracies particle orbits may become stochastic. In our computations numerical stochasticity becomes significant for tracing time spans longer than 2 ms. We, therefore, restrict the quantitative analysis of our numerical results to loss times  $t_{\text{loss}} \leq 2 \text{ ms}$ , for both passing and trapped particles.

Including the magnetic field ripple, approximately 5% more passing particles are lost (mostly particles of #3). However, with respect to the total number of traced passing particles

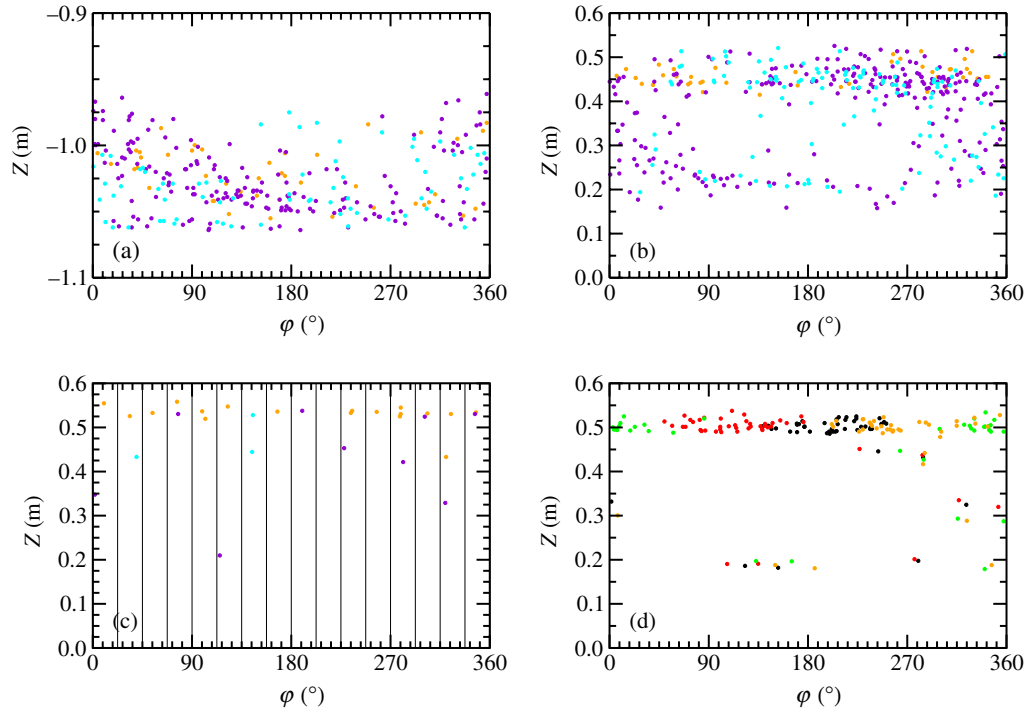


**Figure 10.** Deposition patterns of the lost passing particles on the outer limiting surface: (a) lower divertor region, unperturbed axisymmetric field, (b) low-field side, unperturbed axisymmetric field, (c) low-field side, ripple losses (the vertical lines mark the toroidal positions of the toroidal field coils), (d) low-field side, NTM losses (perturbation 1) of particles of #5 for various island phases (black:  $\phi_{1,2} = 0^\circ$ , red:  $\phi_{1,2} = 90^\circ$ , green:  $\phi_{1,2} = 180^\circ$  and orange:  $\phi_{1,2} = 270^\circ$ ).

this means only an increase of 0.4%. Similar to the magnetic field lines (see figure 4(b)), the ripple causes a toroidally varying radial shift of the drift orbits, which leads to these additional losses. In panels (b) and (c) of figures 9 and 10, we show the initial positions and the deposition patterns of the passing particles which are lost at the low-field side. Figures 9(b) and 10(b) present the pure axisymmetric case, whereas figures 9(c) and 10(c) show the initial positions and deposition patterns of particles additionally lost due to the field ripple. Compared to the particles lost in the lower divertor region (figure 9(a)), the initial positions (figures 9(b) and (c)) of these particles are located a little more inside the plasma boundary, around the  $q = 4$  flux surface. Their deposition patterns cover the whole toroidal circumference (see figures 10(b) and (c)). Furthermore, the pattern of the particles additionally lost due to the field ripple reflects the toroidal characteristics of the ripple. In figure 10(c), the vertical black lines indicate the toroidal positions of the 16 toroidal field coils. As expected, most of the particles hit the outer wall in toroidal positions centred between two coils. There, the toroidal magnetic field has its minimum, and the radial outward shift of field lines and guiding centres is maximal.

In order to distinguish ripple induced passing particle losses from losses caused by NTMs, we consider perturbed fields (perturbations 1 and 2) without ripple. In figures 8(b) and (c) typical drift orbits are presented for perturbation 1. Due to the relatively high perturbation at the plasma boundary, drift orbits in this region are stochastic (outer orange dots in figures 8(b)



and (c)). We should note that the magnetic field is already slightly stochastic in this region, as shown in figure 5(a). Furthermore, the formation of (4,1)-drift islands leads to additional losses. As illustrated in figure 8(b), the (4,1)-drift islands intersect the outer limiting wall at the low-field side. Particles which start at the inner side of the drift island move around the island (see also the enlargement of the guiding centre orbits shown in figure 8(c)), which leads to a radial shift equivalent to the drift island width. The studies provide clear evidence that this shift is responsible for the NTM induced passing particle losses in the case of the considered AUG discharge. Figure 9(d) presents the initial distribution of these additionally lost particles. Their initial positions are located between the  $q = 3$  and 4 flux surfaces. Of course, the deposition pattern of these lost particles depends on the phase of the drift islands. For example, figure 10(d) shows the deposition pattern of the additionally lost particles of #5. Note, here the colours mark the island phases  $\phi_{1,2} = 0^\circ, 90^\circ, 180^\circ$  and  $270^\circ$ . The deposition patterns clearly reflect the  $90^\circ$  phase shift of the islands. This strong phase dependence agrees very well with the experimental results [12], where a strong correlation between the frequency and the phase of the (2,1)-NTM and those of the passing particle losses has been observed.

The amount of the NTM-induced losses depends on the island phase. We, therefore, calculate the phase angle averaged losses. The losses caused by perturbation 1 are #3: 0.32%, #5: 2.08% and #7: 0.46% of the total number of passing particles. This corresponds to an increase of lost passing particles of #3: 9.30%, #5: 15.91% and #7: 17.39% with respect to prompt passing particle losses in the axisymmetric field. The same calculations for perturbation 2 show an increase of only #3: 1.74%, #5: 3.78% and #7: 0%. That is, many fewer particles are additionally lost in case of perturbation 2, because there the plasma boundary region is almost unperturbed (see also figures 5(c) and (d)). For both perturbations, the (2,1)-drift islands are located inside the plasma boundary and they are hardly stochasticized (i.e. see figures 8(b) and (c)). They play no role for the passing particle losses within the considered time period of 2 ms.

#### 4.3. Trapped particle losses

In the considered unperturbed axisymmetric equilibrium no losses of trapped particles are observed, if particle collisions are neglected and stochastic diffusion due to numerical field errors is negligible (the tracing time is limited to 2 ms). The magnetic field ripple may cause trapped particle losses by stochastic diffusion and/or ripple well trapping [1, 2]. Here only trapped particle losses induced by stochastic diffusion are observed. As illustrated in figure 11(a), the perturbation near the turning points of a trapped particle leads to an almost vertical displacement of the turning point position, and the particle starts to diffuse in the radial direction. The performed simulations for the first 2 ms show the following results. In the case of the unperturbed field with ripple the losses are 1.7 and 8.7% for #3 and #5, but no particle losses can be seen for #7. This can be explained as follows. Fast ions injected by #3 and #5 have smaller parallel velocities than particles injected by #7 (see section 4.1, figure 6). Therefore, the turning points of the latter particles are mostly located on the high-field side, where the field ripple is small. However, the particles of #3 and #5 have their turning points mostly on the low-field side, where the field ripple is high (see figure 4(a)).

All lost trapped particles are initially localized at the low-field side close to the plasma boundary (see figure 12(a)). Their deposition pattern at the outer limiting wall shows a modulation caused by the field ripple, as illustrated in figure 13(a). As in case of the passing particles, they hit the wall preferentially between the positions of the toroidal field coils.



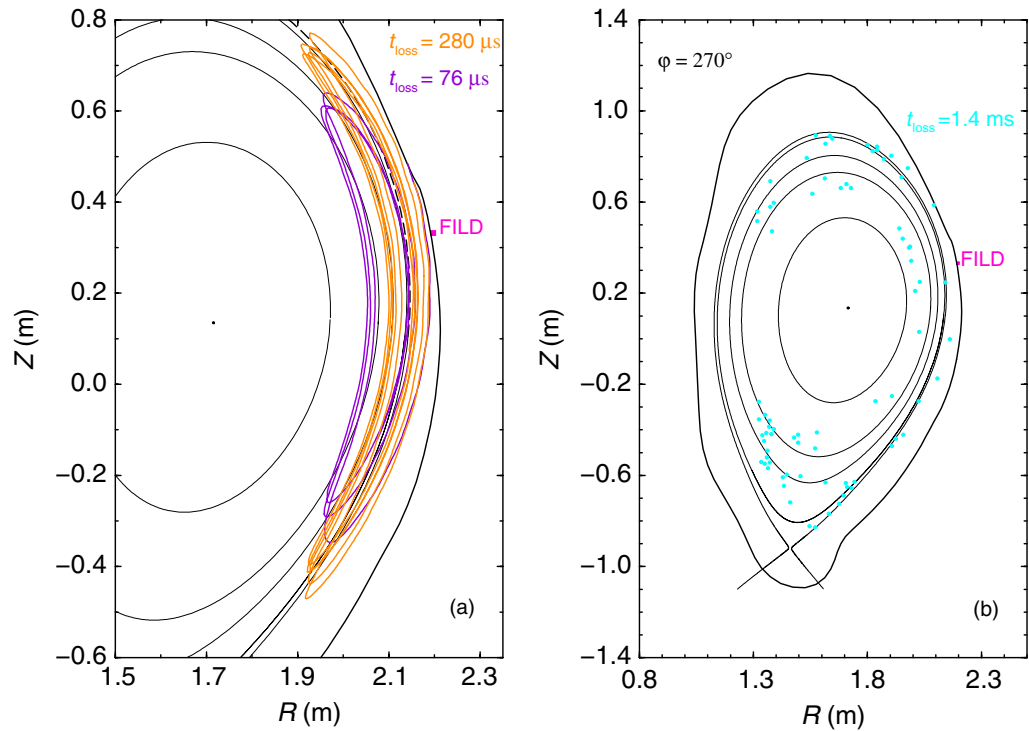


**Figure 11.** Poloidal projection (a) and Poincaré plot (b) of characteristic guiding centre orbits of trapped particles (coloured lines and points) in the (a) unperturbed field with ripple and, (b) the perturbed field (perturbation 1) without ripple. The black lines show unperturbed rational flux surfaces, the separatrix and the outer limiting surface.

In the considered time period, the NTM is mainly responsible for losses of particles originating from #7. In contrast to the case with field ripple, 1.8% of the reflected particles of #7 and almost no particles of #3 and #5 are lost. Furthermore, we obtain similar results for perturbations 1 and 2. Particle trajectories allow a deeper insight into the underlying processes. As indicated by figure 11(b), the field perturbations cause a stochastic diffusion of the position of the turning point of these particles.

Again the initial positions of these particles are localized around the plasma boundary at the low-field side (see figure 12(b)). Figure 13(b) shows the deposition pattern of lost particles of #7 for various island phases. The toroidal location of the deposition pattern slightly depends on the island phase, but this dependence is not as pronounced as in case of the passing particles (see figure 10(d)) because of the stochasticization of the trapped particle orbits. This is in agreement with the experimental observations [12].

Furthermore, we observe a transition from barely passing particles to trapped particles caused by the field perturbation. The total number of trapped particles increases by 3.76% (#3), 3.68% (#5) and 12.37% (#7) for perturbation 1, and 3.14% (#3), 3.03% (#5) and 8.87% (#7) for perturbation 2. The effect is smaller for perturbation 2 because of the reduced perturbation amplitude in the outer plasma region.

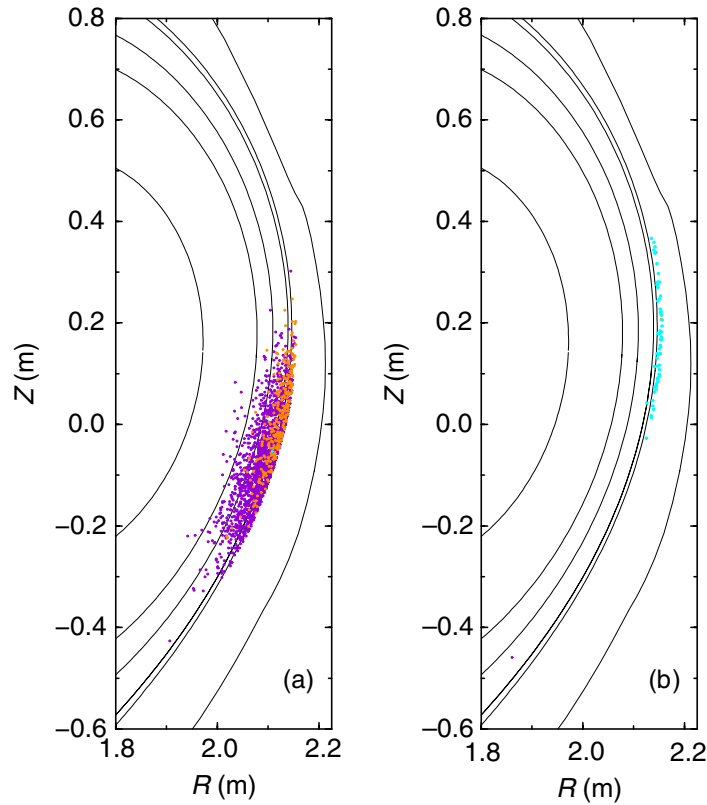


**Figure 12.** Poloidal projection of the initial distributions of the lost trapped particles: (a) unperturbed field with ripple, (b) perturbed field (perturbation 1) with ripple. The black lines show unperturbed rational flux surfaces, the separatrix, and the outer limiting surface.

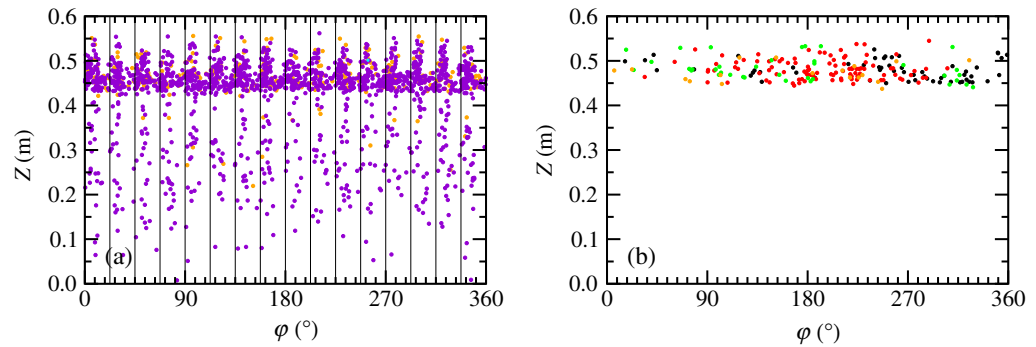


**Figure 13.** Deposition patterns of the lost trapped particles on the outer limiting surface: (a) low-field side, ripple losses (the vertical lines mark the toroidal positions of the toroidal field coils), (b) NTM losses (perturbation 1) of particles of #7 for various island phases (black:  $\phi_{1,2} = 0^\circ$ , red:  $\phi_{1,2} = 90^\circ$ , green:  $\phi_{1,2} = 180^\circ$  and orange:  $\phi_{1,2} = 270^\circ$ ).

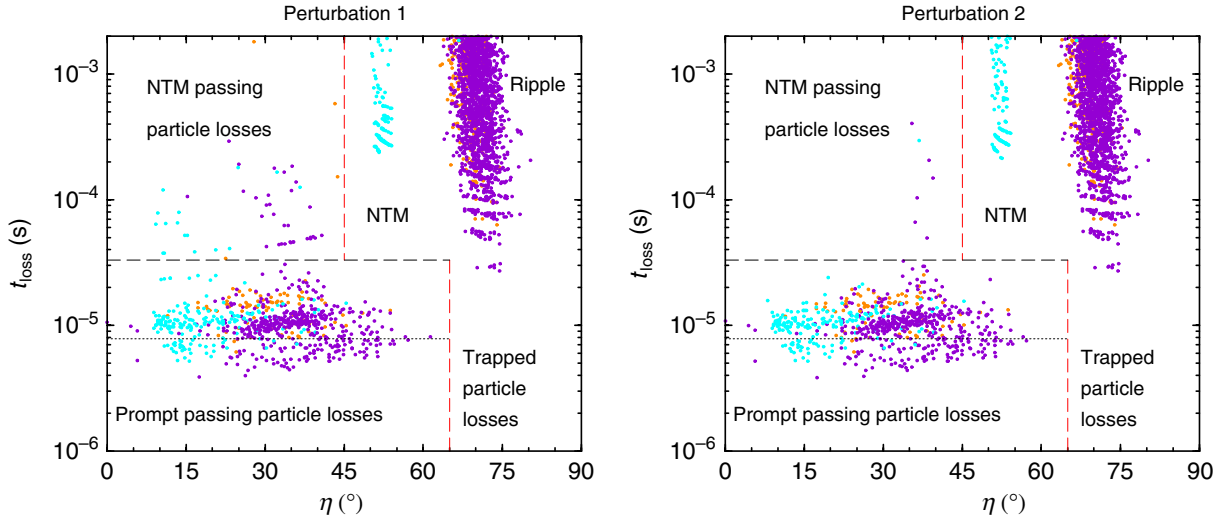


**Figure 14.** Distributions of the lost particles with respect to pitch angle,  $\eta$ , and loss time,  $t_{\text{loss}}$ , for (a) perturbation 1, and (b) perturbation 2. The vertical, red dashed lines separate the passing (left) from the trapped (right) particle losses, while the black, dashed horizontal line separates the prompt passing particle losses (bottom) from NTM-induced losses (top). The black, dotted horizontal line marks approximately the boundary between prompt passing particles intersecting the outer limiting surface in the lower divertor region (bottom), and the particles intersecting the wall at the low-field side (top).

#### 4.4. Total losses

The total losses of the passing and trapped particles are summarized in figures 14 and 15. Figures 14(a) and (b) show the distribution of loss time versus pitch angle for perturbations 1 and 2, and the field ripple. A comparison of both figures illustrates that mainly the passing particle losses caused by the NTM are different for the two perturbations. As already discussed in section 4.2, these losses are predominantly caused by the (4,1)-drift islands, which are larger in the case of perturbation 1. For this particular ASDEX Upgrade equilibrium the loss times can be summarized as follows: (i) prompt passing particle losses:  $t_{\text{loss}} \leq 35 \mu\text{s}$ , (ii) NTM passing particle losses:  $t_{\text{loss}} \approx 40\text{--}200 \mu\text{s}$ , (iii) ripple losses of trapped particles:  $t_{\text{loss}} \geq 35 \mu\text{s}$ , and (iv) NTM trapped particle losses:  $t_{\text{loss}} \geq 200 \mu\text{s}$ . A comparison of these timescales with the estimated slowing down and total deflection rates (see section 2) shows that collision processes play no essential role. However, on longer timescales they will have to be taken into account.

Finally, figures 15(a)–(d) present the lost particle distributions with respect to gyroradius,  $\rho$ , and pitch angle,  $\eta$ . The distribution of the prompt passing particle losses (at the low-field side) without ripple and perturbation is shown in figure 15(a). The pattern is divided into three stripes because of the discrete particle energies of  $E = 93 \text{ keV}$  (top),  $60 \text{ keV}$  (middle) and  $41.5 \text{ keV}$  (bottom). The distribution of the additionally lost passing particles due to the NTM is illustrated in figure 15(b). The distributions for ripple and NTM-induced trapped particle losses are presented in figures 15(c) and (d), respectively. In figure 15(c) the particle energies of the various stripes are 93, 60, 41.5, 30, 31 and 20 keV, and 93, 41.5 and 30 keV (from top to bottom) in figure 15(d). These computed distributions are in qualitative agreement with the

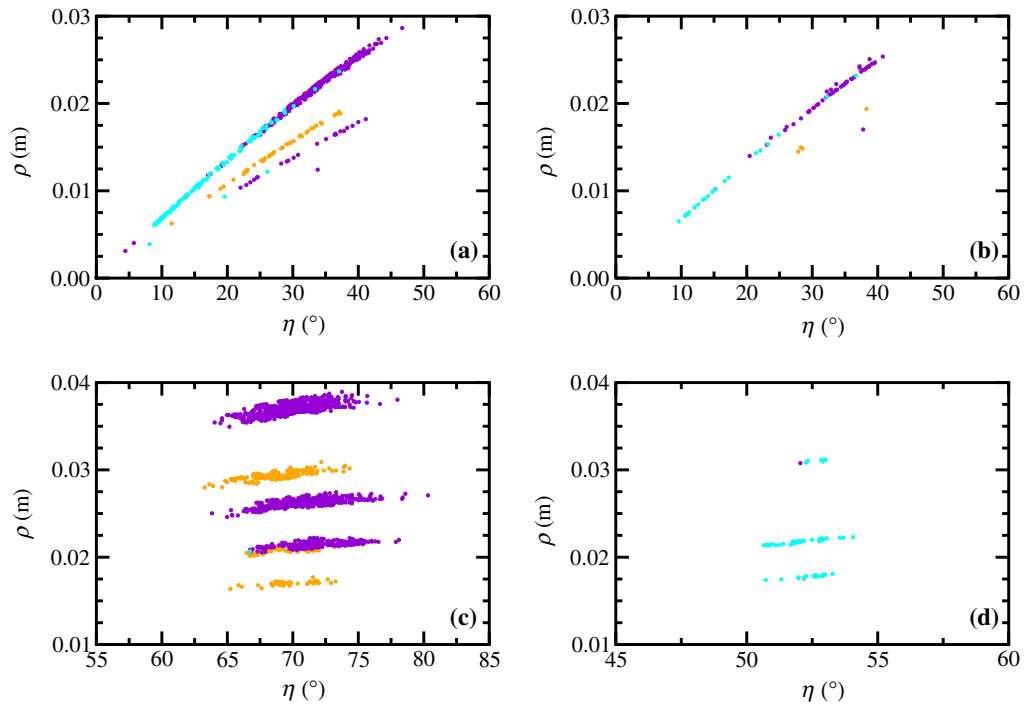


**Figure 15.** Distributions of the lost trapped particles with respect to gyroradius,  $\rho$ , and pitch angle,  $\eta$ : (a) prompt passing particle losses, (b) NTM-induced passing particle losses (perturbation 1), (c) ripple losses of trapped particles, and (d) NTM-induced losses of trapped particles (perturbation 1).

patterns obtained with the FILD measurements published by Garcia-Muñoz *et al* in [12]. There, in figure 2 (page L11), a CCD picture is presented showing the distribution of the measured lost particles as a function of pitch angle and gyroradius.

Although the numerical studies have been made under very realistic conditions, one has to be aware of the fact that nonetheless the following effects have not been taken into account: (i) Only guiding centre orbits are traced. That is, the finite gyroradius, which is in the order of a few centimetres for this kind of particle, is not taken into account. (ii) The complicated 3D structure of PFCs is approximated by an axisymmetric, closed surface. (iii) Only a very few of the approximately 100 000 traced particles hit the outer limiting wall in the region where the fast ion detector is located (bad statistics). (iv) Energy and pitch angle scattering, as well as island rotation, have been neglected. However, the importance of these effects is beyond the scope of this paper, but will be a subject of future investigations.

## 5. Summary

We have studied fast particle losses of a (2,1)-NTM unstable ASDEX Upgrade equilibrium (discharge #21089,  $t = 4$  s) within the first 2 ms. The magnetic islands caused by the NTM instability have been simulated by adding perturbation fields to the equilibrium field. Unlike the numerical studies presented in [12], here (i) the real equilibrium geometry has been used, (ii) the magnetic field ripple has been taken into account, (iii) the tracing of the guiding centres

of the fast ions has not been limited to the plasma region (see also discussion below), but has been carried out up to the PFCs, (iv) the deposition patterns of the lost fast particles on the PFCs have been determined, and (v) the particle collisions have been neglected. For this ASDEX Upgrade discharge we have identified the following loss mechanisms: (i) prompt passing particle losses, (ii) NTM-induced passing particle losses caused by (4,1)-drift island formation, (iii) ripple losses of trapped particles due to stochastic diffusion, (iv) NTM-induced trapped particle losses also caused by stochastic diffusion. Here, a significant stochasticization of the drift islands, which exceeds the stochasticization of the magnetic field, could not be observed. Most of the passing particles have been lost within  $35 \mu\text{s}$  (prompt losses), and  $400 \mu\text{s}$  (NTM-induced losses), respectively. The first trapped particle losses set in after  $35 \mu\text{s}$ . The fast ions injected by #3 and 5 have been mostly lost due to the magnetic field ripple, while the more parallel injected ions of #7 have hardly been affected by the ripple. However, the (2,1)-NTM mode has caused trapped particle losses of the latter in the order of 2% ( $t_{\text{loss}} \leq 2 \text{ ms}$ ). Within the considered time period of 2 ms, only particles originating from regions close to the plasma boundary have been lost. On longer timescales, energy and pitch angle scattering processes as well as the stochastic orbits of the trapped particles would lead to additional losses from the interior of the plasma.

It should be noted that the number of lost particles, loss times, deposition patterns and also the identified loss mechanisms depend sensitively on the position and shape of the outer limiting wall, the plasma equilibrium (i.e.  $q$ -profile, field ripple) and the field perturbation. It is very important to locate the plasma-facing components a realistic distance from the plasma boundary. A restriction of the calculations to the region inside the plasma boundary inevitably leads to an overestimate of the loss rate. For instance, all passing particles which follow drift orbits that intersect the plasma boundary would be lost within a very short time period. Furthermore, our calculations have shown that the used field perturbation (e.g. vanishing or non-vanishing perturbation in the plasma boundary region) strongly influences the NTM-induced particle losses. All these results underline the importance of using a realistic equilibrium, perturbation and wall geometry input for the simulations.

Although the prompt and ripple losses have dominated the NTM-induced ones in the considered case, NTMs may cause severe fast particle losses for other configurations and discharges. In our case the (2,1)-NTM located at half of the plasma radius did not cause a significant stochasticization of the drift islands. In discharges where the  $q = 2$  is located far more outside (e.g. at 80% of the plasma radius), and the particle energies are much higher (e.g. in the case of ITER), a (2,1)-NTM may lead to a stochasticization due to the overlap of drift islands, and to an enhanced loss of fast particles.

## Acknowledgments

We thank M Garcia-Muñoz, V Igochine, M Maraschek, P Martin and M Reich for many fruitful discussions about the experimental results, and for providing the initial particle distribution (M Garcia-Muñoz) and the ASDEX Upgrade shotfile (M Reich).

## References

- [1] Goldstone R J and Towner H H 1981 *J. Plasma Phys.* **26** 283
- [2] Goldstone R J, White R B and Boozer A H 1981 *Phys. Rev. Lett* **47** 647

- [3] Mynick H E and Duvall R E 1989 *Phys. Fluids B* **1** 750
- [4] Wong K L *et al* 1991 *Phys. Rev. Lett.* **66** 1874
- [5] Heidbrink W, Strait E J, Doyle E, Sager G and Snider R T 1991 *Nucl. Fusion* **31** 1635
- [6] Garcia-Muñoz M *et al* 2008 *Phys. Rev. Lett.* **100** at press
- [7] Sigmar D J, Hsu C T, White R D and Cheng C Z 1992 *Phys. Fluids B* **4** 1506
- [8] Ye H, Berk L H and Breizman B N 1991 *Bull. Am. Phys. Soc.* **36** 2393
- [9] Zweben S J *et al* 1999 *Nucl. Fusion* **39** 1097
- [10] Zweben S J *et al* 2000 *Nucl. Fusion* **40** 91
- [11] Carolipio E M, Heidbrink W W, Forest C B and White R B 2002 *Nucl. Fusion* **42** 853
- [12] Garcia-Muñoz M *et al* 2007 *Nucl. Fusion* **47** L10
- [13] Mynick H E 1993 *Phys. Fluids B* **5** 1471
- [14] Mynick H E 1993 *Phys. Fluids B* **5** 2460
- [15] Putvinsky S V 1990 *JETP Lett.* **51** 642
- [16] Garcia-Muñoz M 2006 Fast response scintillator based detector for MHD induced energetic ion losses in ASDEX Upgrade *PhD Thesis* Ludwig-Maximilian-University, Munich
- [17] Konovalov S V and Putvinsky S V 1990 *Fusion Technol.* **18** 397
- [18] Bittoni E and Haegi M 1992 *Fusion Technol.* **22** 461
- [19] Schneider W, McCarthy P J, Lackner K, Gruber O, Behler K, Martin P and Merkel R 2000 *Fusion Eng. Des.* **48** 127
- [20] McCarthy P J, Martin P and Schneider W 1999 The CLISTE Interpretive Equilibrium Code *Max-Planck-Institut für Plasmaphysik Technical Report* IPP 5/85
- [21] Hirshman S P and Lee D K 1986 *Comput. Phys. Commun.* **39** 161
- [22] Hirshman S P, van Rij W I and Merkel P 1986 *Comput. Phys. Commun.* **43** 143
- [23] Strumberger E 1997 *Nucl. Fusion* **37** 19
- [24] Strumberger E, Merkel P, Schwarz E and Tichmann C 2002 MFBE.2001: computation of magnetic fields of ideal MHD equilibria *Max-Planck-Institut für Plasmaphysik Laboratory Report* IPP 5/100 Online at [http://www.ipp.mpg.de/ippcms/de/kontakt/bibliothek/ipp\\_reports/index.html](http://www.ipp.mpg.de/ippcms/de/kontakt/bibliothek/ipp_reports/index.html)
- [25] Igochine V, Dumbrajs O, Constantinescu D, Zohm H, Zvejnieks G and the ASDEX Upgrade TEAM 2006 *Nucl. Fusion* **46** 741
- [26] Yu Q 2006 *Phys. Plasmas* **13** 062310
- [27] Gourdon C 1970 *Programme Optimise de Calculs Numeriques Dans le Configurations Magnetique Toroidales* CEN, Fontenay aux Roses
- [28] Strumberger E 2000 *Nucl. Fusion* **40** 1697
- [29] McGuinness H and Strumberger E 2004 GEOM: discrete geometric mapping for toroidal devices *Max-Planck-Institut für Plasmaphysik Laboratory Report* IPP 5/109 Online at [http://www.ipp.mpg.de/ippcms/de/kontakt/bibliothek/ipp\\_reports/index.html](http://www.ipp.mpg.de/ippcms/de/kontakt/bibliothek/ipp_reports/index.html)
- [30] Lister G G 1985 A fully 3D neutral beam injection code using Monte Carlo methods *Max-Planck-Institut für Plasmaphysik Technical Report* IPP 4/222